Mass Flux and Vertical Distribution of Currents Caused by Strong Winds in a Wave Tank

TOSHINORI OGASAWARA AND TAKASHI YASUDA

Department of Environment and Renewable Systems, Gifu University, Gifu, Japan

(Manuscript received 28 October 2003, in final form 5 April 2004)

ABSTRACT

The velocity fields of wind-driven currents under strong winds were measured in a wind-wave tank with a double bottom. The tank has the characteristics to satisfy partially the continuity of the mass flux and to reduce return-flow effects on the currents. The lower part of the double-bottom tank functions as a duct to circulate the currents, allowing the measurement of the return-flow velocity. The velocity measurements were made on the currents just below the mean water level by using a high-resolution particle image velocimetry (PIV) system and tracking floats and on the currents inside of the duct by using a normal PIV system. Thus, accurate data of the vertical distribution and mass flux of the currents driven by strong winds were obtained from the PIV data. As a result, it is found that the flux in the surface layer with the thickness of 2 times the significant wave height amounts to about 30% of the total mass flux of the currents driven by strong winds with a reference wind speed of 12.0 m s^{-1}.

1. Introduction

Wind-driven currents play important roles in the transport of suspended solids and sediment, planktons, and dissolved oxygen. In particular, the currents driven by strong winds due to unusual meteorological disturbances, such as typhoons or cold fronts, not only can cause coastal disasters, but also can have a great influence on coastal environments. This is because the currents in the coastal sea and inner bays can become not only the primary cause for storm surge and large-scale beach changes, but also a trigger for a great change of water quality and the ecosystem.

Many field observations have been performed to investigate the vertical distribution of the wind-driven currents, particularly that in the water surface layer, because the currents in the wave-affected surface layer have great influence on various transportation phenomena, air–sea interaction, and so on. Kitaigorodskii et al. (1983) carried out observations on the velocity field affected by wind speeds exceeding 10 m s^{-1} and pointed out that the surface layer with enhanced turbulence is extended down to about 10 times the wave amplitude and its layer does not obey the law of the wall. Thorpe (1992) also reported similar results based on the interpretation of acoustic reflections from bubbles. Also, Gargett (1989) inferred a dissipation rate decaying faster than the first-power decay of distance below the surface, from vertical-profile measurements. However, usual field observations lack information on the velocity field in the surface layer affected by developed wind waves accompanying breakers because of the difficulty of the measurements. Therefore, tank experiments are required inevitably to obtain the necessary information under desirable conditions.

Tank experiments allow high-accuracy measurements of near-surface velocity fields of the currents driven by strong winds under various controlled conditions. However, since experiments using a conventional closed-end wind-wave tank suffer from return flow induced by reverse pressure gradient, which is balanced with the wind stress together with the shear stress of the bottom and sidewalls, they cannot give the velocity information on the currents driven by wind stress alone. This problem was already pointed out by Lin and Gad-el-Hak (1984). They developed a wind-wave tank with a false bottom installed at 15 cm above the original bottom tank to satisfy the continuity of the mass flux and to minimize the reverse flow effects, and measured velocity profiles of mean surface currents driven by the wind speed of 10 m s^{-1}. However, because the tank was too short to generate wind waves accompanying whitecaps, the velocity profiles were measured under nonbreaking wind waves. Wang and Wu (1987) developed a circulation wind-wave tank of doughnut type without return flow and measured the water particle velocity below wind waves using a laser Doppler velocimeter (LDV). However, their measurements also lacked information on ve-

Corresponding author address: Dr. Toshinori Ogasawara, Department of Civil and Environmental Engineering, University of Iwate, 4-3-5 Ueda, Morioka Iwate 020-8551, Japan.
E-mail: togasa@iwate-u.ac.jp

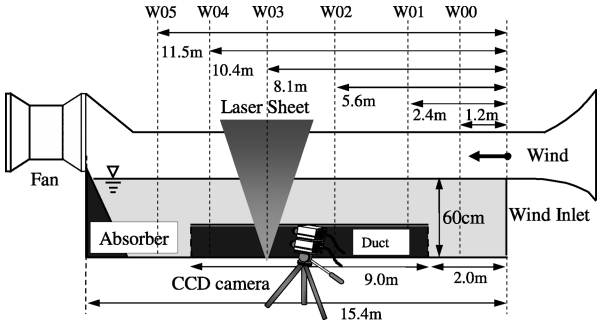

FIG. 1. Wind-wave tank with double bottom and measuring locations.

locity of currents driven by strong winds because the experiments were carried out under the moderate wind speed of 6.4 m s^{-1}. Cheung and Street (1988) measured the mean velocity of currents driven by a strong wind of 13.1 m s^{-1} speed in a straight wind-wave tank 35 m long with closed ends using an LDV. Their results showed that the currents under the surface layer obey the logarithmic law, but they did not include data on the velocity field just below the mean water level.

Thus, the inevitable requirements to investigate the vertical distribution of near-surface currents driven by strong winds arise with respect to the deduction of the influence of return flow on wind-driven current velocities, and the development of the measuring technique to obtain the velocity data just below the mean water level.

In this study, the experiments to satisfy the aforementioned requirements were conducted by using a double-bottom tank, similar to that proposed by Lin and Gad-el-Hak (1984), and a PIV system specialized for high-speed flows. The vertical distribution and total mass flux of the currents driven by strong winds were accurately determined.

2. Experiments

a. Experimental apparatus and method

Laboratory experiments were performed using a wind-wave tank 15.4 m long, 0.4 m wide, and 1.0 m deep. The tank comprises all-glass sidewalls and bottom to allow flow visualizations. At the ends of the tank, spaces of 2.0 and 4.4 m are left between the upper bottom and the end walls, as illustrated in Fig. 1, to guide the return flow under the upper bottom and reduce its influence on the wind-driven currents. The space between the upper and lower bottoms functions as a duct to circulate the currents as return flow, allowing one to measure the velocity of the return flow, which is only disturbed by the reverse pressure gradient within the tank.

The inner height h_c of the duct was set to change from 0 to 29 cm; $h_c = 0$ cm states that the tank is a conventional wind-wave tank, called here a single-bottom tank.

The reference wind speed U_r at the entrance of the wind tunnel ranged from 3.0 to 15.1 m s^{-1} and was measured with a Pitot–static tube with electronic differential manometers. The measurement point of U_r was fixed at a height of 20.0 cm above the still water level.

Water-surface elevations were measured with capacitance-type wave gauges, which were adapted for wind-wave tank use and located at the four measuring points from W01 to W04 shown in Fig.1. They were recorded for 180 s and sampled at the frequency of 100 Hz. The mean water levels at the measuring points W00 and W05 were monitored by ultrasonic displacement sensors. They were the time-mean values of water-surface elevations at both of the points recorded for 90 s.

The aerated water-surface current velocity was measured by tracking floats passing two stations 1.5 m upwind and downwind, respectively, from the location of W02. The floats used are similar to those mentioned by Wu (1975) and consist of a columnar cork with a diameter of 1.0 cm, a height of 1.5 cm, and a normal metal stem to change the height of the gravity center.

The water particle velocity fields were visualized by using nylon particles with a diameter of 50 μm and a relative density of 1.02 as tracers. The nylon particles were irradiated from the tank floor with a 5-W-power green-light laser sheet about 5 mm thick. Their images were captured with two synchronized cameras of 125 frames per second (fps) rate and 480 $\times$ 480 pixel resolution. Although the recording time of each run was 16.7 s, the captured images enabled us to measure high-speed velocity fields immediately below the mean water level. The velocity fields were examined by means of the particle image velocimetry (PIV) analysis described in section 2c.

b. Experimental conditions

The measurements were run for various wind speeds generating from ripples to fully developed wind waves as shown in Fig. 2. The still water depth h was set to 60.0 cm during the experiments. The experimental conditions are listed in Table 1. Figure 3 shows the relationships between the wind wave spectra at the location of W03 and the reference wind speeds from $U_r = 3.3$ to 12.0 m s^{-1}. All of the frequencies f_p indicating the spectral peaks shift down and all of the spectral values $S_\eta(f_p)$ at f_p develop with increasing of wind speeds. It could be confirmed that the spectral values $S_\eta(f > f_p)$ in a higher frequency band than the peak frequency f_p obey the power law of f^{-4}.

In the case of $U_r = 3.3$ m s^{-1}, ripples were merely generated on the water surface. In the case of $U_r = 6.7$ m s^{-1}, moderately developed wind waves were generated, but no whitecaps could yet be observed because of the short fetch. However, when the wind speed U_r reached 10.4 m s^{-1}, whitecaps were partly formed

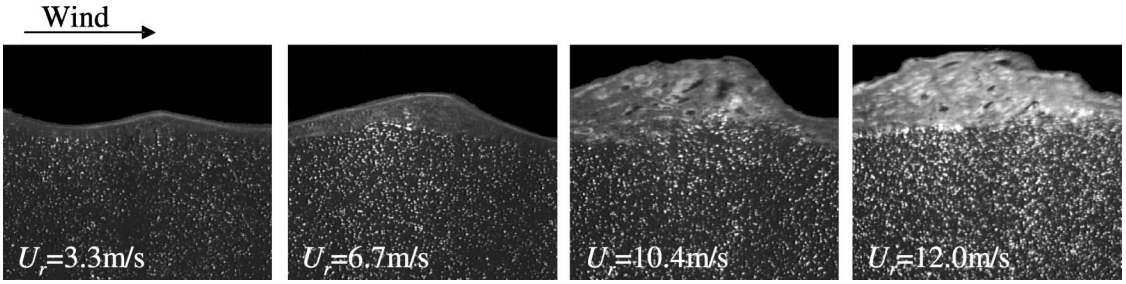

FIG. 2. Spatial water surface at the location of W03 affected by the wind with speed U_r from 3.3 to 12.0 m s^{-1}.

around the location of W03. Then, in the case of U_r = 12.0 m s^{-1}, all of the wave crests formed whitecaps at the location of W03. To quantify the amount of whitecaps, Ogasawara et al. (2002) suggested a wind-wave breaker index based on the thickness of the air-bubble mixing layer and showed that the breaker rate δ of each wave crest in the present wind-wave tank could be treated as follows: $\delta \leq 3\%$ at U_r = 6.7 m s^{-1}, $\delta \approx 23\%$ at U_r = 10.4 m s^{-1}, and $\delta \approx 50\%$ at U_r = 12.0 m s^{-1}.

Figure 4 shows the relationships between wave spectra in the wind-wave tank at U_r = 12.0 m s^{-1}. It is found that the spectral value $S_\eta(f_p)$ at f_p develops and the peak frequency f_p downshifts with increasing of fetch. However, the developing rate of the wave spectra from W02 to W04 becomes lower because wave breaking begins around the location of W03.

On the assumption that the vertical distribution of horizontal wind speeds above the water surface obeys the logarithmic law, the values of the friction wind velocity u_{*a} were determined by applying the least squares method to the present laboratory wind speed data. Figure 5 shows the relationship between the values of u_{*a} derived and to the reference wind speed U_r. A solid line is drawn with the following empirical equation proposed by Wu (1980):

$$u_{*a}^2 = (0.8 + 0.065U_r) \times 10^{-3}U_r^2 \ (\text{m}^2\ \text{s}^{-2}). \quad (1)$$

Since the present experimental data of u_{*a} cover various water surface states from ripples to the whole whitecaps and they fairly agree with the solid line, the values of u_{*a} given by Eq. (1) were employed here as the air-side friction velocity in terms of the reference wind speed U_r.

c. PIV analysis

Two kinds of PIV analyses were applied for the calculation of the water particle velocity. One is a direct cross-correlation method (Direct-CCM), which is applicable for high-speed and intensively fluctuating velocity fields affected by breaking waves but requires a long processing time. The other is the FFT cross-correlation method (FFT-CCM), which is not suitable for breaking-wave-affected fields although it does not require a long processing time since it utilizes the FFT code. Therefore, FFT-CCM was applied to low-speed velocity fields not affected by breaking waves because the processing time is short in comparison with that of Direct-CCM.

Figure 6 shows the temporal variation (t = 9–10 s) of vertical distribution of the velocity vectors below the mean water level at the location of W03, analyzed by the Direct-CCM. The water surface position was extracted from the images previously shown in Fig. 2, and then the mean water level was determined by averaging it for the recording time of 16.7 s. Although the temporal variation of the velocity vectors shows that the wave component is dominant over the depth in comparison with the other ones such as mean flows and eddy motions, they exhibit that fast flow with the direction of wind is generated in the surface layer from mean water level to depth $z \approx -2$ cm.

It should be taken into account here that the visualization images of the surface layer that captured the wave trough might contain false velocity information because there is no water flow between the mean water level and the wave trough. In the case of U_r = 12.0 m s^{-1}, water always flows below the depth $z = -3$ cm and all the visualization images completely capture the water flow. However, in the depth -3 cm $< z \leq -1$ cm, the number of the visualization images capturing water flow is reduced to about 80% of the 2048 continuous images, that is, about 1650 images. Further, in the depth -1 cm $\leq z < 0$ cm, it decreases to about 60% of them, that is, about 1250 images. Therefore, the

TABLE 1. Experimental conditions at the measuring location W03.

U_r (m s^{-1})	u_{*a} (m s^{-1})	H_S (cm)	T_S (s)	f_p (Hz)	$S_\eta(f_p)$ (m^2 s)
3.3	0.11	1.1	0.02	3.6	0.08
6.7	0.24	3.0	0.37	2.8	0.86
10.4	0.40	5.5	0.49	2.1	3.83
12.0	0.48	6.6	0.54	1.8	5.69

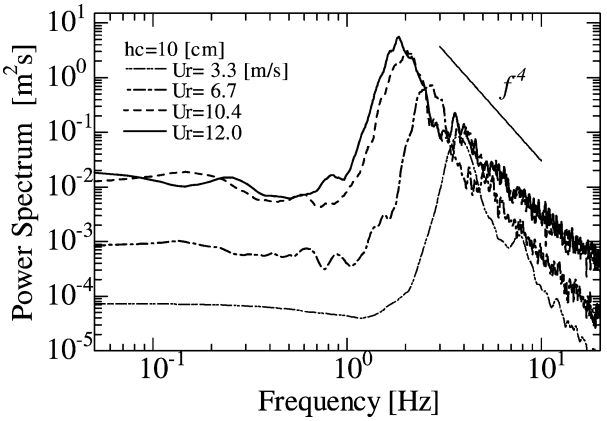

FIG. 3. Relationship between wave spectra S_η at the location of W03 and wind speeds U_r from 3.3 to 12.0 m s^{-1}.

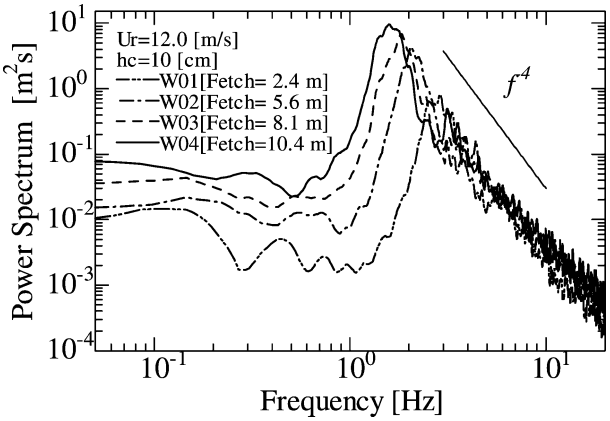

FIG. 4. Relationship of wave spectra S_η and fetch in the case of U_r = 12.0 m s^{-1}.

time-averaged velocities $\overline{u}$ were calculated by using the images captured below the depth of $z \approx -1$ cm and the following PIV method.

Therefore, the validity of $\overline{u}$ thus calculated should be examined. Figure 7 shows the comparison of the vertical distribution of horizontal mean velocity at the wind speed U_r = 12.0 m s^{-1} among the values of $\overline{u}$ analyzed by the Direct-CCM, the FFT-CCM, and those measured by using the tracking floats mentioned in section 2a. The result plotted with solid circles, denoting the values of $\overline{u}$ analyzed by the Direct-CCM, verifies the applicability of the Direct-CCM to high-speed velocity fields immediately below the water surface. On the contrary, the values of $\overline{u}$ analyzed by the FFT-CCM, denoted by open circles, show disagreement in the upper layer (depth ≥ -3 cm). However, since they agree with the values by the Direct-CCM in the lower velocity field (depth ≤ -3 cm), the FFT-CCM with fast processing time becomes applicable.

3. Hydraulic characteristics of a double-bottom tank

a. Difference of mean water levels between both ends of the wind-wave tank

The wind-wave tank used here is basically similar to the tank used by Lin and Gad-el-Hak (1984). The present tank has a double bottom and can circulate wind-driven currents to the upwind end as return flow through a duct. Hence, it could partially satisfy the mass continuity of the current. However, since both ends of the tank are closed as in conventional tanks with a single bottom, the hydraulic characteristics of this tank are supposed to be intermediate between the circulating wind-wave tank used by Wang and Wu (1987) and single-bottom tanks. Therefore, the hydraulic characteristics are difficult to predict and need to be investigated in detail.

Figure 8 shows the relationship of the reference wind speed U_r and the difference Δh inducing return flow between the mean water level at the locations W00 and W05. The relationship covers inner heights of the circulation duct from h_c = 0 to 29 cm and shows that the values of Δh are proportional to the wind speed U_r alone and are almost independent of the value of h_c. This shows that the difference of the mean water level at both ends is determined uniquely by the wind stresses.

b. Vertical distribution of horizontal mean velocity

Figure 9 shows comparisons of the vertical distribution of horizontal mean velocity $\overline{u}$ at the wind speed of U_r = 10.4 m s^{-1} among wind-wave tanks with duct heights h_c = 0, 8.0, and 19.0 cm. It is noted that the presence of the double bottom (h_c = 8 and 19 cm) results in a remarkable difference of the values of $\overline{u}$ of the currents inside of the duct as compared with those in the corresponding lower part of a single-bottom tank (h_c = 0 cm). Further, it should be emphasized that the maximum velocity $\overline{u}_{\max}$ of the currents inside of the duct is quite independent of its height h_c and is governed only by the value of Δh. This result suggests that the

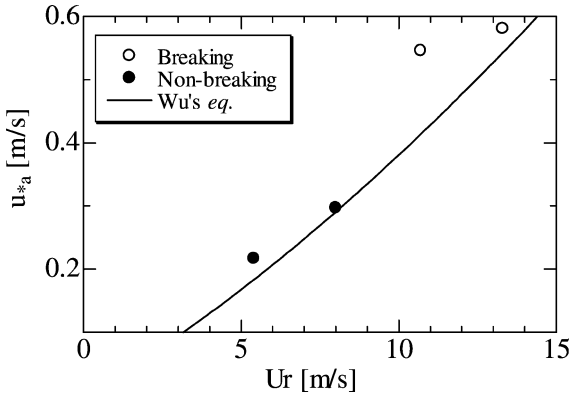

FIG. 5. Relationship between the air-side friction velocity u_{*a} and the reference wind speed U_r.

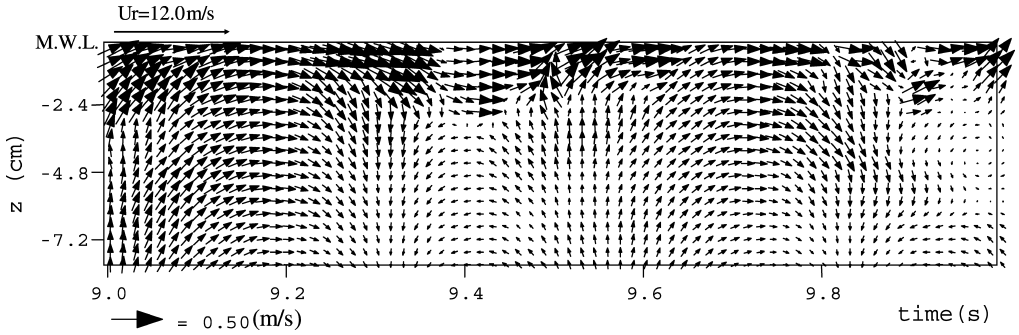

FIG. 6. Temporal variation of vertical distribution of the velocity vectors analyzed by the Direct-CCM below the mean water level at the location W03.

value of $\overline{u}_{\max}$ agrees with the velocity of friction-free return flow generated only by the pressure gradient between both ends of the tank and the currents, except that flows near top and bottom walls of the duct correspond to the pure return flow.

c. Return flow and total mass flux

Since the value of $\overline{u}_{\max}$ obtained by the measurement of the current velocity inside of the duct gives the velocity of the pure return flow, as mentioned above, it should agree with that of the mean velocity of return flow U_B given by vertically averaging $\overline{u}(z)$ of which velocity components near top and bottom walls were eliminated,

$$U_B = \frac{1}{h_c}\int_{-h_b}^{-h_t} \overline{u}(z)\, dz, \tag{2}$$

where $h_t \approx h - h_c$, $h_b \approx h$, and $\overline{u} \approx \overline{u}_{\max}$. If the flow inside of the duct could be treated as friction free, the value of U_B should agree with that of $\overline{u}_{\max}$.

Figure 10 shows the relationship of the mean velocity U_B to the wind speed U_r in double-bottom tanks with four duct heights. The solid line denotes the regression straight line drawn by the following equation:

$$U_B = -1.2 \times 10^{-2} U_r \ (\mathrm{m\ s^{-1}}). \tag{3}$$

It is evident that the values of U_B are independent of the values of the duct height h_c and increase in proportion to the wind speed U_r. Moreover, the total mass flux q_T of the wind-driven currents, which so far have been unknown because the return flow compensates the currents driven by wind stress, was determined as $q_T = -U_B h$; its values are denoted on the right-side coordinate of Fig. 10. The values of q_T become proportionally larger with increasing wind speed U_r regardless of the existence of breaking waves. In addition, it is noted that the values of q_T corresponding to the wind speed U_r are useful to determine the whole vertical distribution of the wind-driven currents from the mean water level to the bottom.

4. Vertical distribution of wind-driven currents in the surface layer

a. Vertical distribution and mass flux of currents in the surface layer

The velocity of return flow, induced by the mean water level difference Δh between both ends of the tank,

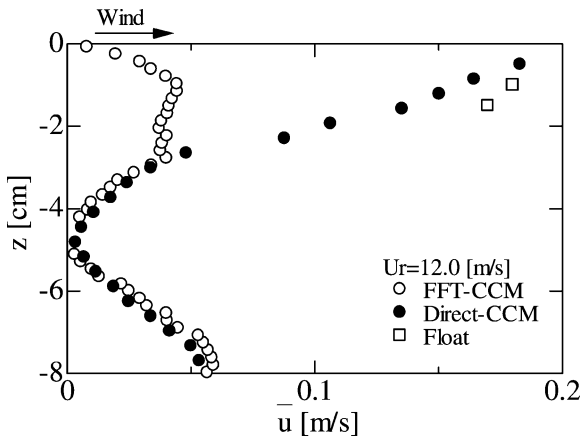

FIG. 7. Comparison of the vertical distribution of horizontal mean velocity $\overline{u}$ among the Direct-CCM, the FFT-CCM, and the tracking floats at wind speed $U_r = 12.0$ m s^{-1}.

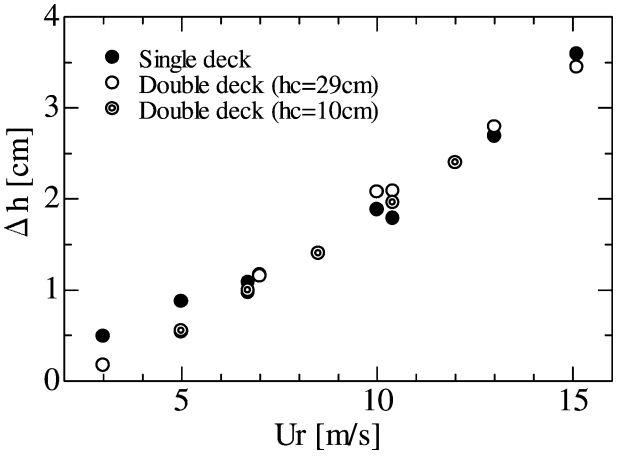

FIG. 8. Relationship of the reference wind speed U_r and the difference Δh between the mean water level at the locations of W00 and W05.

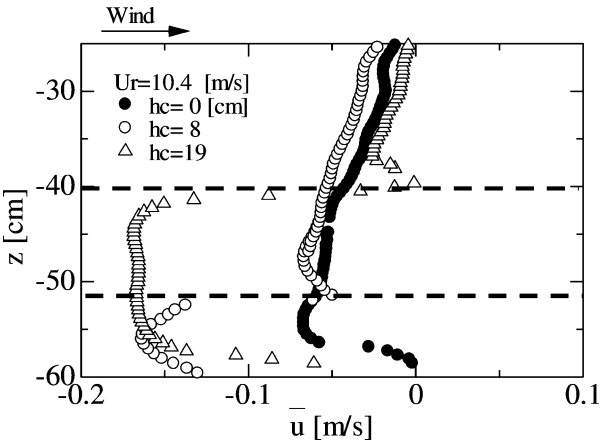

FIG. 9. Comparison of the vertical distribution of horizontal mean velocity $\overline{u}$ at wind speed $U_r = 10.4$ m s^{-1} among wind-wave tanks with duct heights of $h_c = 0$, 8.0, and 19.0 cm.

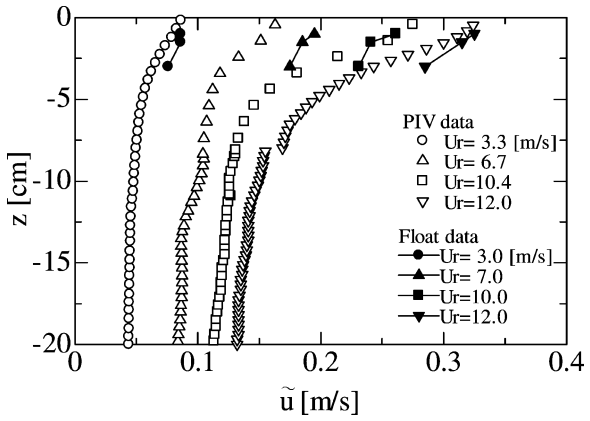

FIG. 11. Comparison of the vertical distribution of the mean velocity between pure wind-driven currents $\tilde{u}$ measured using PIV and surface drift currents U_S measured by tracking floats.

should be distributed vertically uniform and its value should be given as U_B, if the flow could be treated as friction free and the wall friction of the tank were negligible. If the value of U_B is measurable and subtracted from the experimental value of $\overline{u}$ directly obtained through the PIV analysis, the vertical distribution of the pure wind-driven currents without being affected by the return flow become evident and could be represented by the numerically modified velocity $\tilde{u}(= \overline{u} - U_B)$ under the assumption of friction free.

The vertical distribution of the mean velocity $\overline{u}$ obtained with this expression is compared with the surface drift current velocity U_S measured by tracking the floats; this comparison is shown in Fig. 11. The values of U_S and $\tilde{u}$ exclude the influence of the return flow by subtracting the value of U_B from the original mean velocity of the floats. They include both Stokes drift, due to the coupling between horizontal water particle velocity and water surface elevation, and the surface roller flux due to breaking waves, but they are not explicitly included in $\tilde{u}$ defined in the Eulerian coordinates. Nevertheless, the values of U_S agree well with those of $\tilde{u}$ over the entire range of wind speeds from $U_r = 3.3$ to 12.0 m s^{-1}. This result suggests that the influence of the Stokes drift and the surface roller flux on the floats' motion below the mean water level are negligible. The values of $\tilde{u}$ grow larger with the increase of the wind speed U_r and become rapidly larger toward the water surface from the depth of about 2 times the significant wave height H_S in the case of $U_r = 10.4$ and 12.0 m s^{-1}, where whitecaps are generated. Therefore, the vertical distribution of $\tilde{u}$ should be considered to reflect the distribution of the downward-transferred momentum flux supplied through breaking waves. The mass flux q_η in the surface, which thickness η is defined as 0.5, 1, and 2 times the significant wave height H_S, that is, $\eta = -0.5H_S$, $-H_S$, and $-2H_S$, is calculated as

$$q_\eta = \int_\eta^0 \tilde{u}(z)\, dz. \tag{4}$$

Figure 12 shows the relationship between the ratio q_η/q_T, where q_η is the mass flux in the surface layer

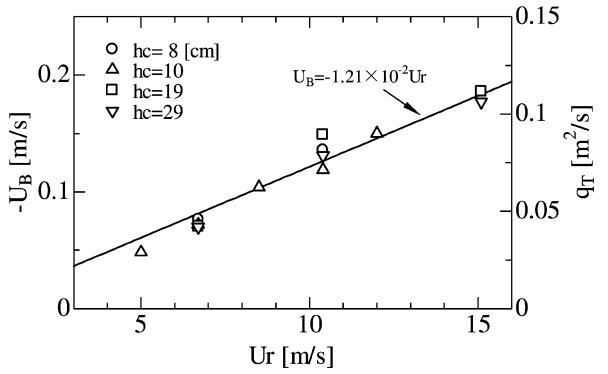

FIG. 10. Relationship among the mean velocity U_B of return flow (coordinate on the left), the wind speeds U_r, and the total mass flux q_T of the wind-driven currents (coordinate on the right) to U_r.

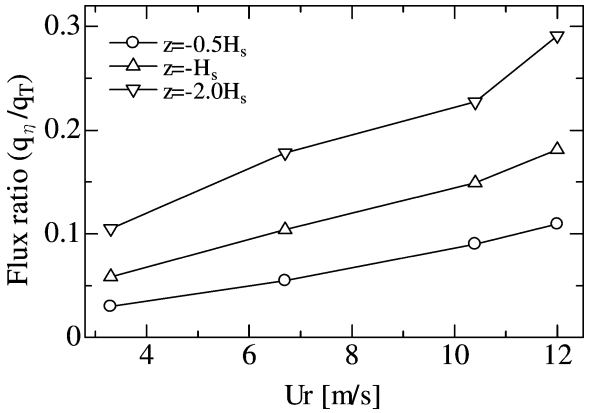

FIG. 12. Relationship between the ratio q_η/q_T (mass flux in the surface layer and total mass flux) and wind speed U_r.

TABLE 2. Values of the parameters of logarithmic and power laws.

U_r (m s^{-1})	u_s (m s^{-1})	u_{*w} (m s^{-1})	z_0 (cm)	α	β
3.3	0.09	0.44×10^{-2}	0.3	—	—
6.7	0.16	0.90×10^{-2}	0.5	—	—
10.4	0.13	1.11×10^{-2}	7.0	0.25	−0.29
12.0	0.14	1.12×10^{-2}	12.2	0.32	−0.32

and q_T is the total mass flux, and the wind speed U_r. In all cases, the values of q_η/q_T become larger with increasing wind speed U_r. Particularly, in the case of $U_r = 12.0$ m s^{-1}, the mass flux q_η in the surface layer with thickness $\eta = -2H_S$ reaches about 30% of the total mass flux q_T, and its mass flux ratio q_η/q_T is almost equivalent to 3 times that when $U_r = 3.3$ m s^{-1}. Hence, the momentum transfer from breaking waves to the mean flow is supposed to be significantly exerted on the development of the wind-driven currents in the surface layer.

b. *Vertical distribution model of wind-driven currents in the surface layer*

The vertical distribution of the horizontal mean velocity of the wind-driven currents was formulated by applying the least squares method to the experimental data of $\tilde{u}$ shown in Fig. 11. As a result, the following equations obeying respectively a power law and a logarithmic law were derived as

$$\tilde{u}(z) = \alpha(z + h)^\beta \quad \text{and} \tag{5}$$

$$\tilde{u}(z) = u_s(z) - \frac{u_{*w}}{\kappa} \log\left(\frac{z}{z_0}\right), \tag{6}$$

where z_0 is the water-side roughness length, which indicates the depth of the intersection between the velocity $\tilde{u}$ described by Eq. (5) and that by Eq. (6), u_s is the value of $\tilde{u}$ at the depth of $z = z_0$, u_{*w} is the friction velocity for water side, and κ (=0.41) is von Kármán's constant. The values of the power-law parameters α and β are indicated together with those of u_s, u_{*w}, and z_0 in Table 2.

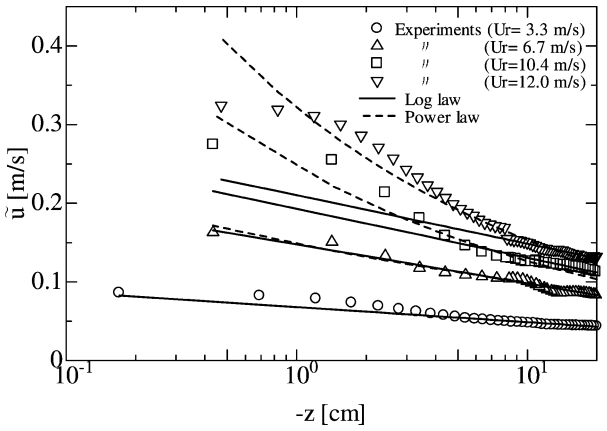

FIG. 13. Comparison of the vertical distribution of $\tilde{u}$ near the water surface between the curves of the power and logarithmic laws at the respective wind speeds U_r.

Figure 13 shows the comparison of the vertical distribution of $\tilde{u}$ near the water surface between the power and logarithmic curves drawn by Eqs. (5) and (6), respectively, and the experimental data. The comparison is made for wind speeds U_r from 3.3 to 12.0 m s^{-1}. In the case of $U_r = 3.3$ m s^{-1}, the experimental data agree well with the logarithmic-law curve over the whole depth and never indicate the formation of a wave-affected (i.e., nonlogarithmic) layer just below the water surface because ripples are merely generated on the water surface. Although wind waves in the case of $U_r = 6.7$ m s^{-1} are in development, they do not accompany whitecaps and the experimental data are still in good agreement with the logarithmic curve until the mean water level. In the case of $U_r = 10.4$ m s^{-1}, where the formation of whitecaps begins around the location of W03, the experimental data close to the mean water level are far apart from the logarithmic-law curve but become in good agreement with the power-law curve. Then, in the case of $U_r = 12.0$ m s^{-1}, the experimental data begin to separate from the log curve near the depth $z = -10$ cm and start obeying the power-law curve for shallower depths. These results show that the power-law layer is formed just below the water surface accompanying whitecaps as previously found by Kitaigorodskii et al. (1983), and its thickness z_0 grows larger with increasing wind speed U_r.

The value of $\tilde{q}_T$ does not contain the mass fluxes of q_{SD} and q_{SR}. It is therefore necessary to include their values into that of $\tilde{q}_T$ when a comparison between $\tilde{q}_T$ and q_T is made. The mass flux q_{SD} due to Stokes drift caused by the interference between water particle velocity and water-surface elevation is approximately calculated by the following equation:

$$q_{SD} = \frac{1}{8} kcH_S^2 \coth(kh), \quad \text{with}$$

$$c = \frac{gT_S}{2\pi} \quad \text{and} \quad k = \frac{4\pi^2}{gT_S^2}, \tag{7}$$

where k is the wavenumber, g is the acceleration of gravity, T_S is the significant wave period, and c is the wave celerity.

Under the assumption that the roller at each wave crest with the time interval of about T_S is transported with the wave celerity c, the value of q_{SR} is calculated

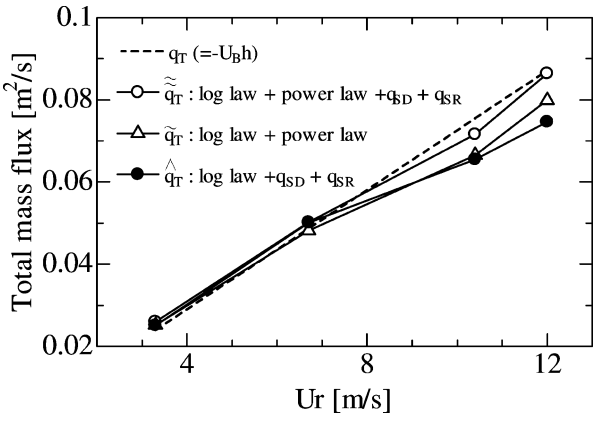

FIG. 14. Relationship of q_T ($=-U_B h$), $\tilde{q}_T$, $\tilde{\tilde{q}}_T$, and $\hat{q}_T$ with wind speed U_r.

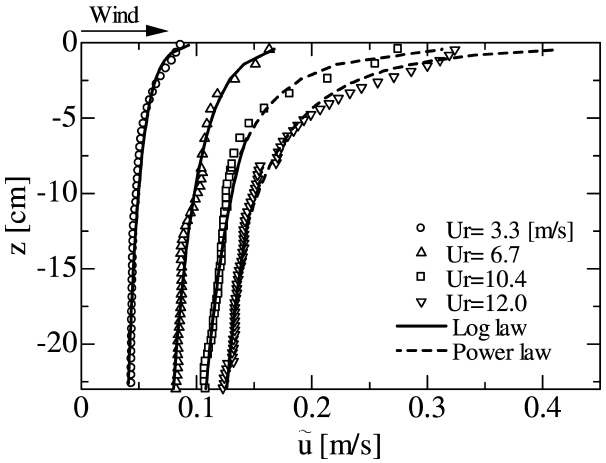

FIG. 15. Vertical distribution of the horizontal mean velocity $\tilde{u}$ of wind-driven currents formulated by the logarithmic and power laws at respective wind speeds U_r.

by the following equation based on Duncan's model (1981):

$$q_{\mathrm{SR}} = \frac{A}{T_S}, \quad \text{with}$$

$$A = \frac{0.015c^4}{g^2 \sin^2\theta} \quad \text{and} \quad \theta = 15^\circ, \tag{8}$$

where A is the area of the surface roller. Thus, the total mass flux $\tilde{\tilde{q}}_T$ including q_{SD} and q_{SR} is defined as

$$\tilde{\tilde{q}}_T = \int_{-z_0}^{0} \alpha(z + h)^\beta \, dz + \int_{-h}^{-z_0} \left(u_s - \frac{u_{*w}}{\kappa} \log\frac{z}{z_0} \right) dz + q_{\mathrm{SD}} + q_{\mathrm{SR}} = \tilde{q}_T + q_{\mathrm{SD}} + q_{\mathrm{SR}}. \tag{9}$$

Moreover, in order to investigate the effects of the power-law layer formation on the total mass flux, the flux $\hat{q}_T$ excluding the existence of the power-law layer is defined as

$$\hat{q}_T = \int_{-h}^{0} \left(u_s - \frac{u_{*w}}{\kappa} \log\frac{z}{z_0} \right) dz + q_{\mathrm{SD}} + q_{\mathrm{SR}}. \tag{10}$$

Hence, it could be said that the difference between $\tilde{\tilde{q}}_T$ and $\hat{q}_T$ indicates the increment of the mass flux due to the formation of the power-law layer.

Figure 14 shows the difference among respective relationships of q_T, $\tilde{q}_T$, $\tilde{\tilde{q}}_T$, and $\hat{q}_T$ to U_r. In the cases of $U_r = 3.3$ and 6.7 m s^{-1}, all values are almost the same and the effects of the power-law layer formation, the Stokes drift, and the surface roller on the total flux are almost negligible. However, for the wind speed $U_r = 10.4$ m s^{-1}, where the formation of whitecaps begins, the values of $\tilde{q}_T$ and $\hat{q}_T$ keep apart from that of q_T although they are the almost same. This result states that the effect of the power-law layer formation on the total flux is of the same order as those of q_{SD} and q_{SR}, and both of them are not necessarily negligible. In the case of $U_r = 12.0$ m s^{-1}, the values of $\tilde{q}_r$ and $\hat{q}_T$ keep apart not only from that of q_T but also from each other, and only the value of $\tilde{\tilde{q}}_T$ coincides with that of q_T. These results state that the effects of the power-law layer formation, the Stokes drift and the surface roller on the total mass flux of wind-driven currents are not negligible, and Eq. (9) taking into account their effects should be applied to describe the vertical distribution of the currents driven by strong winds as shown in Fig. 15.

5. Conclusions

Laboratory experiments to investigate the vertical distribution and mass flux of currents driven by strong winds were performed using a double-bottom tank having a duct for return flow without suffering from wind and breaker stresses. Velocity measurements using a PIV system specialized for high-speed flows and tracking floats made evident the vertical distribution of the mean currents in the surface layer accompanying notable whitecaps and the mass flux of the currents. The mean velocity of the currents entirely obeys the logarithmic law under wind waves without accompanying whitecaps, but under developed wind waves accompanying whitecaps it obeys the power law in the near surface. In the surface layer affected by strong winds, the mean velocity of the currents obeys the power law, the power-law layer develops with the growing of whitecaps, and its thickness reaches about $2H_S$ when the wind speed is $U_r = 12.0$ m s^{-1}. The flux in the surface layer with the thickness of $2H_S$ amounts to about 30% of the total mass flux of the currents driven by strong winds. This states that the surface layer affected by wind-wave breakers plays a very important role in the transport phenomena in the upper ocean under strong winds.

Acknowledgments. This research work was supported by Sasakawa Scientific Research Grant from The Japan Science Society and by Japan Science Society and Grant-in-Aid for Scientific Research 16360243 from Japan Society for the Promotion of Science.

REFERENCES

Cheung, T. K., and R. L. Street, 1988: The turbulent layer in the water at an air–water interface. *J. Fluid Mech.,* **194,** 133–151.

Duncan, J. H., 1981: An experimental investigation of breaking waves produced by a towed hydrofoil. *Proc. Roy. Soc. London,* **377,** 331–348.

Gargett, A. E., 1989: Ocean turbulence. *Annu. Rev. Fluid Mech.,* **21,** 419–451.

Kitaigorodskii, S. A., M. A. Donelan, J. L. Lumley, and E. A. Terray, 1983: Wave–turbulence interactions in the upper ocean. Part II: Statistical characteristics of wave and turbulent components of the random velocity field in the marine surface layer. *J. Phys. Oceanogr.,* **13,** 1988–1999.

Lin, J. T., and M. Gad-el-Hak, 1984: Turbulent current measurements in a wind-wave tank. *J. Geophys. Res.,* **89,** 627–636.

Ogasawara, T., M. Takeda, and T. Yasuda, 2002: Wind wave breaker index based on air-bubbles mixing layer thickness. *Proc. Coastal Eng.,* **49,** 331–335.

Thorpe, S. A., 1992: Bubble clouds and the dynamics of the upper ocean. *Quart. J. Roy. Meteor. Soc.,* **118,** 1–22.

Wang, J., and J. Wu, 1987: Effects of near-bottom return flows on wind-induced currents. *J. Phys. Oceanogr.,* **17,** 2263–2271.

Wu, J., 1975: Wind-induced drift currents. *J. Fluid Mech.,* **68,** 49–70.

——, 1980: Wind-stress coefficients over sea surface near neutral conditions. *J. Phys. Oceanogr.,* **10,** 727–740.